MorphoCellSorter: An Andrews plot-based sorting approach to rank microglia according to their morphological features.

Running title: MorphoCellSorter

Sarah Benkeder[1,2], Son-Michel Dinh[2,3], Paul Marchal[1,2], Priscille De Gea[1,2], Muriel Thoby-Brisson[4], Violaine Hubert[1,5], Ines Hristovska[1,2], Gabriel Pitollat[4], Kassandre Combet[1,2], Laura Cardoit[4], Bruno Pillot[1,5], Christelle Léon[1,5], Marlène Wiart[5,6], Serge Marty[7], Jérôme Honnorat[1,2,8], Olivier Pascual[1,2#], Jean-Christophe Comte[1,9 #]

[1] Claude Bernard Lyon 1 University, Lyon, France.

[2] Institut MeLiS, INSERM U1314 CNRS UMR5284, Lyon, France.

[3] Institut National des Sciences Appliquées (INSA), Lyon, France.

[4] Institut de Neurosciences Cognitives et Intégratives d'Aquitaine, CNRS UMR 5287, Université de Bordeaux, Bordeaux, France.

[5] CarMeN Laboratory, INRAE U1397, INSERM U1060, Claude Bernard Lyon 1 University, Lyon France.

[6] CNRS, Lyon, France.

[7] Sorbonne Université, Institut du Cerveau – Paris Brain Institute – ICM, Inserm, CNRS, APHP, Hôpital de la Pitié Salpêtrière, Paris, France.

[8]French Reference Center on Paraneoplastic Neurological Syndromes and Autoimmune Encephalitis, Hospices Civils de Lyon.

[9] Centre de Recherche en Neurosciences de Lyon (CNRL), INSERM 1028 CNRS UMR5292, Bron, France.

[#] Contributed equally

Key words Microglia; Morphology; Andrews plots; Principal component analysis; Ranking; Ischemia; Alzheimer's disease; Development; Neurodevelopmental disease.

Word count: 10620

Abstract

Microglia exhibit diverse morphologies reflecting environmental conditions, maturity or functional states. Thus, morphological characterization provides important information to understand microglial roles and functions. Most recent morphological analysis relies on classifying cells based on morphological parameters. However, this classification is not always biologically relevant, as microglial morphologies constitute a continuum rather than segregated groups. Instead, we propose a new open-source tool, MorphoCellSorter, which assesses microglial morphology by automatically computing morphological criteria, using principal component analysis and Andrews plots to rank cells. MorphoCellSorter accurately ranked cells from various microglia datasets in mice and rats of different age, from *in vivo*, *in vitro* and *ex vivo* models, that were acquired using diverse imaging techniques. This approach allowed for the discrimination of cell populations in various pathophysiological conditions. Finally, MorphoCellSorter offers a versatile, easy and ready-to-use method to evaluate microglial morphological diversity that could easily be generalized to standardize practices across laboratories.

Introduction

In the healthy brain, microglial cells are characterized by a complex arborization of highly ramified and fine processes that are evenly distributed around the cell body. Their processes present a strong and constant dynamic of protractions and retractions. For many years, this dynamic has been associated with their monitoring role, as they are constantly looking for danger signals in their surroundings (Davalos et al., 2005; Nimmerjahn, Kirchhoff, & Helmchen, 2005). Microglia continuously adapt to their local environment, sensing even small changes via membrane receptors and transporters (Hanisch & Kettenmann, 2007). They are able to react quickly and adjust their functions in response to the detected signals. These functional changes are supported by morphological modifications. As an example, the formation of filopodia enables directed migration to lesion sites, while the formation of phagocytic cups and phagolysosome increases are linked to their phagocytic activity (Kettenmann, Hanisch, Noda, & Verkhratsky, 2011; Sierra, Abiega, Shahraz, & Neumann, 2013).

The traditional view of microglia being either ramified (homeostatic microglia) or amoeboid (reactive microglia) has now been proven to be oversimplified and inaccurate, as microglia display a whole range of various morphologies (Paolicelli et al., 2022). Indeed, many studies have shown a wide diversity of microglial morphotypes in pathological conditions, and microglia can even exhibit an increase in ramification within the first hours of injury (Vidal-Itriago et al., 2022).

In stroke models, morphological transformation of reactive microglia is correlated with the severity and duration of ischemia, as well as an enhanced expression of markers such as CD11B and CD68 (Zhang, 2019). In the rodent brain, different morphotypes can be observed depending on how the area has been impacted by the metabolic challenge. Thus, a gradient of microglial morphologies can be observed from amoeboid microglia in the ischemic core to ramified complex cells in the contralateral cortex (Anttila, Whitaker, Wires, Harvey, & Airavaara, 2017; Fumagalli, Perego, Ortolano, & De Simoni, 2013). Similarly, in Alzheimer's disease (AD) mouse models, microglial cells

73 associated with Aβ plaques present strong morphological transformations in opposition to plaque-
74 distant cells mildly morphologically impacted (Plescher et al., 2018).

75 As a matter of fact, morphology is an indicator that is easy to obtain when characterizing a model
76 through live imaging or immunohistochemistry, and it has been used in numerous studies to describe
77 a broad range of pathological contexts (Adeluyi et al., 2019; Ali et al., 2019; Morrison, Young,
78 Qureshi, Rowe, & Lifshitz, 2017; Plescher et al., 2018). To date, the literature contains a wide variety
79 of criteria to quantitatively describe microglial morphology, ranging from descriptive measures such
80 as cell body surface area, perimeter, and process length to indices calculating different parameters
81 such as circularity, roundness, branching index, and clustering or artificial intelligence (AI)
82 approaches to categorize morphologies (Adaikkan et al., 2019; Heindl et al., 2018; Kongsui, Beynon,
83 Johnson, & Walker, 2014; Leyh et al., 2021; Morrison et al., 2017; Young & Morrison, 2018). This
84 variety of metrics and approaches to measure microglia morphology makes it difficult to compare
85 results between studies. Moreover, categorization methods seem subjective with the number, name
86 and composition of categories being non consistent between studies. In addition, as microglial
87 morphology is highly diverse, it is not rare to be confronted with cells belonging to categories that
88 are not defined, or that could belong to several of them.

89 Here, we propose a fully automated program that quickly and unbiasedly computes most parameters
90 used in the literature to characterize microglial morphology, and overcomes the limitations of
91 current methods. Our approach consists in: 1) performing principal component analyses (PCA) to
92 select the parameters best fitted to describe the dataset of interest and 2) generating a sorting of the
93 cells based on their morphology. The originality of our study is the use of Andrews Plots to accurately
94 rank microglia according to their morphology and discriminate distinct populations. In addition, our
95 working flow has been developed so that it can be used for a wide variety of models and image
96 acquisitions (confocal, wide field, two-photon, etc.). We developed this method on an exploratory

97 dataset from a rat brain with focal cerebral ischemia, and validated it on other independent datasets
98 from other models (other animal, age, pathology) to confirm its wide range of application.

99 **Methods**

100 **Models**

101 All experimental procedures were carried out in accordance with the French institutional guidelines
102 and ethical committee, and authorized by the local Ethics Committees of the University of Bordeaux
103 and "Comité d'éthique pour l'Expérimentation Animale Neurosciences Lyon": CELYNE; CNREEA no.
104 42, and the Ministry of National Education and Research (APAFIS#30666-2021032518063894).

105 *Ischemic stroke rat model – fixed tissue*

106 The experiment was conducted on a 6-8-week-old Sprague Dawley rat with transient (90 minutes)
107 middle cerebral artery occlusion (tMCAo) followed by reperfusion. Twenty-four hours after
108 reperfusion, the animal was deeply anesthetized (xylazine at 12 mg/kg and ketamine at 90 mg/kg in
109 0.9% NaCl) and died by the collapse of the lungs when the thoracic cage was open. Infusion of
110 phosphate-buffered saline (PBS) was performed directly in the left ventricle. Next, 100 mL of
111 paraformaldehyde (PFA) 4% was infused at 10 mL/min before the brain collection. The brain was
112 then post-fixed in PFA 4% for 2-4 days, rinsed, and soaked in 30% sucrose for 72 hours before being
113 frozen in -40°C 2-methylbutane. It was then stored at -20°C until being cut. Floating 30 µm thick
114 sections were obtained using an NX50 cryostat and conserved in PB-Thimerosal until
115 immunostaining.

116 *Ischemic stroke mouse model – live tissue*

117 An ischemic stroke was induced in 8 to 12 weeks CX3CR1$^{+/GFP}$ mice by a permanent occlusion of their
118 middle cerebral artery (pMCAo). Imaging was performed the next day directly on living animals
119 through a cranial window. Briefly, animals were anesthetized with isoflurane (induction: 3-4%,

120 surgery: 1.5-2%) and installed on a stereotaxic apparatus where their temperature was monitored
121 and maintained at 37°C. After cleaning and exposition of the skull, a polyamide implant was glued on
122 a zone at the periphery of the lesion in order to be able to image both ischemic and extralesional
123 regions. The skull was then cautiously thinned by drilling until a thickness of 20 to 30 µm was
124 reached. A glass coverslip was then glued to the thinned region. Mice were then put under a heating
125 lamp and individually housed until imaging (V. Hubert et al., 2021).

126

127 *Phox2b mutation and Embryonic dataset*

128 The expansion of a 20-residue polyA tract in PHOX2B is used as a model for Central Hypoventilation
129 Syndrome (CCHS) (Amiel et al., 2003). Mutant pups were generated by mating conditional
130 Phox2b$^{27Ala/27Ala}$ females with Pgk::Cre males (Dubreuil et al., 2008). Since mutant newborns die
131 rapidly after birth, all experiments were performed blind on E18.5 embryos of either sex, and the
132 genotype of each embryo was determined a posteriori on tail DNA. Pregnant mice were killed by
133 cervical dislocation at E18.5. Embryos were rapidly excised from uterine horns and placed in artificial
134 oxygenated cerebrospinal fluid (aCSF) at 18-20°C until dissection. The aCSF solution composition was
135 (in mM): 120 NaCl, 8 KCl, 0.58 NaH2PO4, 1.15 MgCl2, 1.26 CaCl2, 21 NaHCO3, 30 Glucose, pH 7.4 and
136 equilibrated with 95% O_2-5% CO_2. Embryos were decerebrated and decapitated, and ventral tissues
137 were removed. Brainstems were then carefully disassociated from the surrounding tissues and
138 completely isolated by a rostral section made at the junction between the rhombencephalon and
139 mesencephalon and a caudal section at the spinal cord level. After dissection, brainstem
140 preparations were placed in 4% PFA for 2 - 3 h for tissue fixation. To obtain transverse frozen
141 sections, brainstems were placed in a 20% sucrose-PBS solution for cryoprotection overnight, then
142 they were embedded in a block of Tissue Tek (Leica Microsystems, France) and sectioned at 30 µm
143 using a cryostat (Leica Microsystems, France).

144 *Alzheimer's Disease model*

145 C57BL6 5-month-old female APPxPS1-KI and control (PS1-KI) mice were used[25]. For the brain
146 collection, 0.5 mg xylazine was injected intraperitoneally followed by Euthasol. They were then
147 intracardially perfused first with 4% PFA in PB. After one hour, the brains were collected and then
148 post-fixed for 2 hours in 4% PFA and stored in PBS. They were rinsed in phosphate buffer (PB) and
149 soaked in 30% sucrose for 48 hours before being frozen at -40°C in 2-methylbutane for 2 minutes and
150 stored at -70°C until the cut. Free-floating sections (30 µm thick) were cut using a cryostat and
151 conserved in PB-Thimerosal until immunostaining.

152 *In vitro microglia*

153 We followed the protocol published by Bohen and collaborators using Magnetic Activated Cell
154 Sorting (MACS) (Bohlen, Bennett, & Bennett, 2019). Ten days old mice were anesthetized with
155 isoflurane, intracardially perfused with PBS enriched with magnesium and calcium (14040141, Gibco)
156 before decapitation and brain collection. The brains were then finely chopped in a dissociation buffer
157 and transferred to a tissue grinder to dissociate further the cells from the tissue. Myelin and debris
158 were then eliminated thanks to a Percoll® PLUS solution (E0414, Sigma-Aldrich) and an incubation
159 with anti-myelin magnetic beads (130-096-433, Miltenyi Biotec): the cell suspension is applied on a
160 column fixed to a magnet so that the myelin will stay on the column while the cells will exit. To
161 isolate specifically microglia, the suspension was incubated with anti-CD11b magnetic beads (130-
162 097-142, Miltenyi Biotec). Cells were then seeded on 35 mm diameter dishes with 4 compartments
163 with a polymer bottom (80416, Ibidi) coated with poly-D-lysine (100 µg/mL, A-003-E, Sigma-Aldrich)
164 and collagen IV (2µg/mL, 354233, Corning). The culture medium was adapted from Bohlen et al.,
165 2019 with DMEM/F12 (21041025, Gibco), 1% penicillin-streptomycin, 2 mM L-Glutamine (10378016,
166 Gibco), 5 µg/mL N-acetylcysteine (A9165, Sigma-Aldrich), 100 µg/mL apo-transferrin (T1147, Sigma-
167 Aldrich), 100 ng/mL de sodium selenite (S5261, Sigma-Aldrich), 1.5 µg/mL cholesterol (700000P,
168 Avanti), 0.1 µg/mL oleic acid (90260, Cayman Chemical), 1 ng/mL gondoic acid (20606, Cayman
169 Chemical), 1 µg/ml heparan sulfate (AMS.GAG-HS01, AMSBIO), 2 ng/mL TGFβ2 (100-35B, Preprotech)

170 and 10 ng/mL M-CSF (315-02, Preprotech). Cells were kept at 37°C 5% CO_2 and the culture medium
171 was half renewed every two days until imaging (4 to 10 days after seeding).

172 **Immunohistochemistry**

173 The sections underwent 5-minute rinses three times with PBS and Triton 100X 0.3% (PBS-T). Sections
174 from the ischemic experiment were incubated for 20 minutes in a 1.5% hydrogen peroxide solution
175 diluted in PBS, and after 3*10 minutes of rinsing with PBS-T, they were incubated for 30 minutes in
176 0.5% sodium borohydride diluted in PBS and then thoroughly rinsed. One-hour saturation was then
177 performed on all sections with PBS-T, 3% bovine serum albumin and 5% normal goat serum (PBS-T-
178 BSA-NGS). Sections were then incubated overnight with anti-Iba1 antibodies (1/500, Wako, Germany,
179 #W1W019-19741) at 4°C and anti-Amyloid-β 4G8 (1/500, Bio-Legend, #800709) antibody. Sections
180 were rinsed 3*10 minutes the next day with PBS-T. They were then incubated in goat anti-rabbit
181 secondary antibodies coupled with Alexa 555 fluorochrome (1/300, Invitrogen, France, #A21429) and
182 goat anti-mouse coupled with Alexa 488 fluorochrome (1/300, Invitrogen, France, #A11029) for 2
183 hours at room temperature. They were then rinsed 3*10 minutes with PBS and mounted on
184 microscope slides using Fluoromount G (ThermoFisher Scientific, #00-4958-02) and a glass coverslip.

185 For the Phox2b mutant model and embryonic dataset, sections were incubated for 90 min in a
186 solution of PBS containing 0.3% Triton X-100 and 1% BSA to limit nonspecific labeling and favor
187 antibody tissue penetration. The primary rabbit anti-Iba1 antibody (1/500; Wako, Germany,
188 #W1W019-19741) was then applied overnight at room temperature and under slight agitation. To
189 amplify the primary antibody signal, after several washes, sections were incubated with an Alexa
190 Fluor 568 donkey anti-rabbit secondary antibody (1/500, Merck, France, #A10042) for 90 min at
191 room temperature. Immunostained sections were then mounted in Vectashield Hard Set medium
192 (Eurobio, France) cover-slipped and kept in the dark until imaging.

193 **Image acquisitions**

194 For the ischemic stroke model on fixed tissue, acquisitions were performed with a Zeiss confocal
195 microscope and a 40X objective (LSM 880, Zeiss). Z-stacks between 18 and 25 µm thickness were
196 executed with a 1 µm step. For the ischemic stroke model on live, microglia were observed thanks to
197 a two-photon microscope (Bruker Ultima) and a 20X objective, at a deepness of 50 to 150 µm. 10 to
198 15 µm thick acquisitions were acquired with a 1 µm step between plans. For the AD model, a Zeiss
199 Axio Scan 7 microscope slide scanner was used with a 20X objective. Z-stacks (30 µm thick) were
200 performed with a step of 1 µm. For the Phox2b mutant model, imaging was conducted using a Zeiss
201 confocal microscope (LSM 900, Zeiss). Z-stacks (30 µm thick) were performed with a step of 1 µm and
202 a 40X objective. *In vitro* microglia were imaged on a single plane using the BioStation (Nikon).

203 **Image processing and segmentation**

204 The general procedure is described in supplemental Fig. 7.

205 For the ischemic model on fixed tissue, all post-acquisition processing was executed with FIJI
206 software. Individual microglial cells were cropped from the original acquisitions before Z-maximum
207 projections. The brightness of the projections was adjusted, and median (radius=2), mean (radius=2)
208 and unsharp mask (radius=5; mask=0.60) filters were applied via a macro. A threshold was then
209 applied to each crop to binarize the cells, and pixels not belonging to the microglia of interest were
210 manually deleted. The same procedure was performed for the Phox2b mutant model, except the
211 mean filter that was not applied.

212 For the ischemic model on live tissue all post-acquisition processing was also executed with FIJI
213 software. Z-maximum projections were performed, and individual crops of the cells were done.
214 Brightness and contrast of the images were modified before applying a manual threshold to binarize
215 the cells. Reminiscent noise and neighboring cells were manually removed.

216 For the AD model, crops of individual microglial cells located in the secondary visual cortex were
217 generated with *Zen* software and exported to the Tif image format. The next operations were
218 executed with FIJI software. Z stack cleaning was performed by background subtraction (rolling=50),
219 followed by a median filter (radius=3) and an unsharp mask (radius=5; mask=0.60). Segmentation
220 was performed by the FIJI Trainable Weka Segmentation 3D plugin (Arganda-Carreras et al., 2017).
221 The selected training features were based on the Gaussian blur, Laplacian, Maximum, Mean,
222 Minimum, Median and Variance (Minimum sigma: 1.0 and Maximum sigma: 8.0). Binarized z-stacks
223 were then manually cleaned to remove pixels from neighboring cells or remaining noise. Finally, a
224 maximum Z-projection was performed.

225 For the Phox2b mutant model, image processing was performed via a custom MATLAB R2018B
226 (Mathworks, Massachusetts, USA) script. First, a median filter followed by an unsharp mask filter was
227 applied to all images. An automated threshold was then applied. Manual tuning with a thresholding
228 tool (R, 2023) was applied if the automated threshold was not satisfying. The binarized images were
229 then automatically cropped around microglia to manually remove pixels belonging to neighboring
230 cells.

231 For the *in vitro* microglia, acquisitions were cropped around individual microglia, and the cells were
232 then manually traced on Procreate (5.2.9 version).

233 When the binarization process generated one or several holes inside the cell bodies, they were
234 manually filled to not interfere with the automated detection of the cell bodies. All binarized and
235 individualized microglial cells were then rescaled through a FIJI macro command to obtain a pixel
236 resolution equal to 0.5 µm. Finally, the images were resized to obtain a field size equal to 300 x 300
237 pixels.

238 **MorphoCellSorter algorithm pipeline**

239 **Automated measure of 20 dimensionless morphological descriptors**

240 All parameters are illustrated in Supp. Fig. 8.

241 First, we calculate the morphological parameters most commonly used in the literature, followed by
242 other parameters that we have developed and proposed here (Fig. 2B). To make our approach scale-
243 independent, we reformulated some morphological descriptors to obtain dimensionless parameters.

$$Circularity = \frac{2 \times \sqrt{\pi \times CellArea}}{CellPerimeter}$$

$$RamificationIndex = \frac{\frac{CellPerimeter}{CellArea}}{2 \times \sqrt{\pi \times CellArea} \times Image\ length \times Image\ width}$$

$$RoundnessFactor = \frac{4 \times SomaArea}{(Longest\ axis\ length)^2 \times \pi}$$

$$PerimeterAreaRatio = \frac{Perimeter^2}{Cell\ Area}$$

$$Density = \frac{CellArea}{Length \times width\ of\ the\ image}$$

$$Inertia = \frac{Longest\ axis\ length}{Smallest\ axis\ length}$$

244

245 *Cell Body Recognition*

246 The cell body identification is based on successive erosions until the center of the cell body is the
247 only pixels remaining using a 3*3 pixels square as a structuring element. The last erosion is the one
248 preceding the elimination of all pixels belonging to the cell and corresponds to the center of the cell
249 body. Then, successive dilations are performed to reconstruct the cell body according to the
250 morphology of the cells, using a cross (+) 3 pixels height and width (Leyh et al., 2021). Reconstruction
251 of the cell body relies on (1) the identification of the index *i* on which measured surfaces after
252 erosions are inferior to the surfaces measured after dilation, (2) the average of two copies of the
253 images: one on which *i* + 1 erosions have been performed, and the other one on which *i* dilatations
254 have been performed from the center of the cell body. The resulting mean image was then subjected
255 to a threshold fixed at 0.25 to obtain the cell body. From this, we can calculate the following
256 parameters.

$$Processes\ Soma\ Areas\ Ratio = \frac{Processes\ Area}{Soma\ Area}$$

$$Processes\ Cell\ Areas\ Ratio = \frac{Processes\ Area}{Cell\ Area}$$

$$Polarization\ Index = \frac{Soma\ Centroid \mid Cell\ Centroid}{\sqrt{CellArea}}$$

Skeleton

The cell skeleton is obtained via the MATLAB *bwskel* function. This function reduces all 2-D binary objects to 1-pixel width curves while taking care of not changing the essential structure of the image. The aim is to extract the image skeleton while keeping the topology properties such as the Euler number and to extract branchpoints and endpoints. The skeleton length is defined by the number of pixels forming the skeleton minus the pixels of the cell body.

Thus, we calculate the skeleton related parameters:

$$Skeleton\ Process\ Ratio = \frac{(Skeleton\ Length)^2}{Processes\ Area}$$

$$Branchpoints\ Endpoints\ Ratio = \frac{Number\ of\ Branchpoints}{Number\ of\ Endpoints}$$

Sholl analysis

Sholl analysis was performed on the microglial skeleton. Concentric circles with a step size of two pixels were generated on the skeletons minus the soma, and the soma centroid was the center point of the circles. Intersections between the growing circles and the skeleton were counted.

$$Branching\ Index = \sum \frac{(Intersections\ circle_n - \ Intersections\ circle_{n-1}) \times r_n}{\sqrt{Length\ \times width\ of\ the\ image}}$$

Fractal/Hausdorff dimension

The fractal dimension measures the complexity of a cell shape, that is, how an object fills the space at different scales. The Hausdorff fractal dimension (A, 2023) corresponds to the slope of the logarithm of the number of tiles of size ε needed to cover all the surfaces of the object of interest vs the logarithm of ε.

Lacunarity

Lacunarity corresponds to the inhomogeneity of a cell shape. It measures the variance of how the object fills the space at different scales. Patterns with larger gaps generally have higher lacunarity. We used the gliding box algorithm (T, 2023; Tolle, McJunkin, & Gorsich, 2008), and the value corresponds to the slope of the log-log representation.

Convex Hull

The convex hull is the smallest convex polygon (with angles inferior to 180°) enclosing the whole cell.

$$Solidity = \frac{Cell\ Area}{Convex\ hull\ Area}$$

$$Convexity = \frac{Cell\ Perimeter}{Convex\ hull\ Perimeter}$$

$$Convex\ Hull\ Circularity = \frac{2 \times \sqrt{\pi \times Convex\ hull\ Area}}{Convex\ hull\ Perimeter}$$

We also measure the length of the major and minor axes of the convex hull.

$$Convex\ Hull\ Span\ Ratio = \frac{Length\ Major\ axis}{Length\ Minus\ axis}$$

Finally, we measure the largest and smallest radii of the circles from the centroid of the convex hull as the center to external points.

$$Convex\ Hull\ Radii\ Ratio = \frac{Maximum\ Convex\ hull\ radius}{Minimum\ Convex\ hull\ radius}$$

Linearity

A Principal Component Analysis is generated on all the points forming the microglial cell. Then, the variance of the two first principal components (PCs) is calculated; the highest corresponds to the Variance Max and the lowest to the Variance Min.

$$Linearity = \frac{Variance\ Max}{Variance\ Min}$$

Establishment of the cell ranking according to morphological criteria.

The second step is to determine which of the previously calculated parameters best discriminate the cells in a given dataset. Principal component analysis (PCA) is a statistical method allowing dataset dimensionality reduction (Jolliffe & Cadima, 2016). A PCA is performed on the 20 morphological indexes calculated to determine the parameters that best explain the dispersion of the data. Lacunarity, roundness factor, convex hull radii ratio, processes cell areas ratio and skeleton processes ratio were subjected to an inversion operation in order to homogenize the parameters before conducting the PCA: small values for less ramified or more linear cells and higher values for more complex cells less linear. To identify the main parameters responsible for the data spreading, we first transform the raw dataset table into a *z*-scored table by the transformation (1), where $< \tilde{X}_j >$ and $\sigma_{\tilde{X}_j}$ are respectively the average and the standard deviation of the parameter F_j. Because the amplitudes of the parameters are generally very different, such a transformation is necessary to compare their ranges in the same referential.

$$X_{ij} = \frac{\widetilde{X_{ij}} - \widetilde{X_j}}{\sigma_{\widetilde{X}_j}}, \tag{1}$$

We next calculate the parameters correlation matrix, as follow:

$$\mathscr{C}_{XX} = X^T X = \begin{pmatrix} \rho_{1,1} & \rho_{1,2} & \cdots & \rho_{1,n} \\ \rho_{2,1} & \rho_{2,2} & \cdots & \rho_{2,n} \\ \vdots & \vdots & \ddots & \vdots \\ \rho_{m,1} & \rho_{m,2} & \cdots & \rho_{N,N} \end{pmatrix} = \begin{pmatrix} 1 & \rho_{1,2} & \cdots & \rho_{1,n} \\ \rho_{2,1} & 1 & \cdots & \rho_{2,n} \\ \vdots & \vdots & \ddots & \vdots \\ \rho_{m,1} & \rho_{m,2} & \cdots & 1 \end{pmatrix} \tag{2}$$

C_{XX} is a $N \times N$ symmetric square matrix ($\rho_{ij} = \rho_{ji}$, and $\rho_{ii} = 1$) which expresses the correlation between two parameters F_i, F_j taken in pairs. Note that $|\rho_{ij}| \leq 1$. This matrix is comparable to an

inertia tensor of the data cloud. Thus, to find the main directions of the N dimensional data cloud, we calculate the eigenvalues and eigenvectors of C_{XX}, such that:

$$\mathscr{C}_{XX} \, . \, V \; = \lambda \, V. \tag{3}$$

Solving this equation, we get then N eigenvalues $\lambda_1,\ldots,\lambda_N$, each associated to their corresponding eigenvector $V_1,\ldots,V_N$. Each of these eigenvectors has N components. The eigenvector associated with the biggest eigenvalue is the first principal vector or principal component PC_1, while the second principal component PC_2 is the eigenvector corresponding to the immediately smaller eigenvalue $\lambda_2 < \lambda_1$, and so on. Fig. 2B shows an example cascade of eigenvalues in descending order.

PC_1 is the direction in which data are most dispersed, that is the direction holding the most important part of the data information. PC_2 is the second direction holding the next important information part, and so on. The two first components hold almost the whole of information, hence we can consider the plan PC_1, PC_2 as the principal plan reducing the dataset to a two dimensional space. Next, we calculate the projection of the parameters F_n onto the two first principal components respectively PC_1 and $PC2$ (Fig. 2C) and rank those parameters according to the intensity (absolute value) of their projection onto PC_1 (Fig. 2D). Each parameter is then weighted by a factor $W_n = w_n./w_0$, where w_i is the absolute value of the nth parameter projection onto PC_1, and w_0 is the absolute value of the strongest projection among all the parameters. As shown in Fig. 2C, each parameter F_n is represented by a vector in the PC_1, PC_2. Thus, we calculate the projection y_n of each parameter onto PC_2 and calculate the following phase factor $\varphi_i = arctan(y_n/w_n)$.

The following stage of our method consists in introducing the previously calculated factors (Weight: W_n, and phase: φ_n) and their corresponding parameter into a special Fourier synthesis called "Andrews Plot" or "Andrews curve" (Andrews, 1972; García-Osorio & Fyfe, 2005) allowing to visualize

335 the data structure in high-dimensional. The general form of the spectral Fourier synthesis of an

336 individual *j* writes:

$$S_j(t) = \sum_{n=1}^{N} A_n \; cos(2\pi \; n \; t) + B_n \; sin(2\pi \; n \; t) \; , \tag{4}$$

337

338 that we rewrite as,

$$S_j(t) = \sum_{n=1}^{N} C_n \; cos(2\pi \; n \; t \; + \phi_n), \tag{5}$$

339

340 where n, is the index of the ranked parameters, N is the full number of parameters F_n, t is a virtual

341 time $0 \leq t \leq 1$, and $C_n = F_n \times W_n$. Finally, we derive this method to represent data in high dimensional

342 by a simple one-dimension signal composed of orthogonal trigonometric functions in researching the

343 time $t = t^{\boxed{?}}$ for which the curves present the maximum of variance. At this specific time point, we rank

344 individuals according to the magnitude of their own function $S_j(t^{\boxed{?}})$ value as represented Fig. 2E. We

345 now call $S(t^{\boxed{?}})$ the "Andrews-Score".

346

347 **Statistics**

348 Rankings comparisons, performed with Spearman's correlation, were also used to measure the linear

349 correlation between the rankings. They were executed with MATLAB.

350 We used mixed effect models on RStudio, that are adapted to complex experimental designs with

351 dependent and non-dependent data. This allows the addition of random factors to fixed effects.

352 Model fittings and analysis were performed with the lme4 package (Amiel et al., 2003). Condition

353 (Control/APP-PS1xKI or WT/CCHS) was considered a fixed effect, and the factor mice was considered

354 a random intercept. When the mixed models were not applicable, we used Wilcoxon tests. Statistical
355 significance is shown on the graphs (*p < 0.05; **p < 0.01; ***p < 0.001).

356 Number of bins of Andrews scores histograms was automatically determined by the Freedman-
357 Diaconis method based on the following formula:

358 $$k = (x_{max} - x_{min})/(2 \times IQR \times N^{(-1/3)})$$

359 With x_{max} and x_{min} being respectively the maximum and minimum Andrews scores, IQR the
360 interquartile range and N the number of cells.

361 **Results**

362 **Evaluation of classification methods**

363 Morphological categorization has been at the center of recently developed approaches to
364 characterize microglial morphology. It enables the evaluation of the morphological diversity existing
365 in a cell population. Moreover, in the context of morphological comparison between populations, the
366 study of the morphotypes' proportions is relevant as it can highlight meaningful differences that the
367 sole global comparison of morphological criteria cannot. One way to categorize the cells based on
368 their morphology is to perform clustering to group the cells having similar characteristics. We tested
369 a commonly used approach, k-means, to categorize microglia from a rat brain cortex following an
370 occlusion of the middle cerebral artery (Fig. 1A). In this model, microglia contralateral to the lesion
371 are mildly to not impaired whereas ipsilateral microglia undergo light to drastic morphological
372 changes (Anttila et al., 2017; Fumagalli et al., 2013) (Fig. 1A). We selected 20 non dimensional
373 parameters from the literature and developed by the team, on which we conducted a Principal
374 Component Analysis (PCA). The k-means clustering algorithm was applied on the first two principal
375 components (PCs), and we fixed at 4 the number of clusters as commonly chosen in the literature
376 (Verdonk et al., 2016) (Fig. 1B).

377 The obtained microglial groups could be named as ramified microglia (cluster 1), with cells having a
378 morphology consistent with a physiological state. Cluster 2 could be referred to as "activated
379 microglia", as it was composed of microglia displaying various morphologies; they had an
380 intermediary ramification level with large cell bodies. Cluster 3 was composed of cells having few
381 short or no processes and corresponded to amoeboid microglia. Lastly, cluster 4 was rod-like
382 microglia, with two processes extending on either side of the cell body or a single long polarized
383 extension. All the cells of the dataset (ipsilateral and contralateral) and their associated cluster are
384 represented in Fig. 1C. These 4 clusters were not equally represented across each condition as no
385 amoeboid nor rod-like microglia were found in the contralateral side (Fig. 1D). The large majority of
386 the cells were ramified microglia (92%), and the rest were activated microglia (8%). The proportion of
387 ramified cells drastically decreased ipsilaterally by a reduction factor of 4 (23%), while activated
388 microglia increased (39%). 25% of the cells were amoeboid microglia, while rod-like cells represented
389 13% of the ipsilateral population (Fig. 1D). These results show that the microglial populations in each
390 region are different, with microglia having a non-pathological morphology mainly found
391 contralaterally, with only few cells being potentially impacted by the ischemia/reperfusion challenge
392 as they showed morphological signs of reactivity with a less ramified morphology. Ipsilateral
393 microglia were morphologically highly altered, with a decrease in ramified cells, replaced by
394 activated and amoeboid microglia, and rod-like microglia.

395 However, the clusters themselves were highly morphologically heterogeneous, making these
396 quantifications problematic (Fig. 1C). For instance, Cluster 1 (ramified microglia), was composed of
397 cells with branched processes but also included cells that were visibly affected by the ischemic lesion,
398 exhibiting sometimes short, few, or less branched processes, as well as elongated cell bodies. These
399 microglia might have been more appropriate in Cluster 2 (activated microglia). The composition of
400 the latter is also questionable, with the presence of branched processes that would fit better in the
401 first cluster, or cells with few very short extensions that resemble some cells found in Cluster 3.
402 Several non-bipolar or non-unipolar cells are also found in Cluster 2. Some of these cells not

403 belonging to their affiliated clusters were highlighted by a white cross on Fig. 1C. We tested to
404 decrease or increase the number of clusters with no improvement (data not shown).

405 Other classification methods exist, relying on supervised artificial intelligence (AI) algorithms to
406 identify specific morphotypes. These approaches can have high rates of success (96% for the method
407 developed by Leyh and collaborators (Leyh et al., 2021)), meaning that they are in theory efficiently
408 classifying cells. However, the problems of cells which do not fit in a defined category, or to several
409 categories can be raised. For example, in our dataset we found that about 60% of cells would not
410 belong to any category or belong to several categories. In this context, the way the networks are
411 trained might be very subjective to the experimenter and could influence the results. Moreover,
412 depending on the papers, semantic problems are also met, with similar morphologies having
413 different names or on the contrary same names having different definitions (Choi et al., 2022; Leyh et
414 al., 2021), making the comparisons between studies complicated.

415 We know now that microglial morphology is rather a continuum than closed categories (Paolicelli et
416 al., 2022). That is why we propose a continuous ranking rather than a classification of the cells.

417

418 **Development of a ranking approach based on Andrews plots to order rat fixed microglia in a**
419 **context of ischemic stroke lesion.**

420 We developed MorphoCellSorter, a novel ranking method, on the same dataset of rat microglia in
421 the context of an ischemic stroke lesion, on fixed tissue acquired *via* confocal imaging. This model is
422 known to induce major morphological modifications in microglia (Violaine Hubert et al., 2021),
423 enabling us to constitute a heterogeneous dataset, with varied morphologies ranging from amoeboid
424 to hyper-ramified.

425 The method is summed up on Fig. 2A, and takes as inputs binarized and individualized cells form
426 projected Z stacks. To generate the ranking, we first gathered 20 morphological indices, that we also

427 call parameters, either from the literature (Clarke, Crombag, & Hall, 2021; Fernández-Arjona,
428 Grondona, Granados-Durán, Fernández-Llebrez, & López-Ávalos, 2017; Madry et al., 2018) or
429 developed by the team (see Methods). These parameters, describing morphological complexity
430 (circularity, ramification index, roundness factor, perimeter area ration, density, processes soma area
431 ratio, processes cell area ration, skeleton processes ratio, branchpoints endpoints ratio, fractal
432 dimension, lacunarity, solidity, convexity, convex hull circularity, convex hull radii ratio and branching
433 index), linearity (linearity, convex hull span ratio, inertia) and directionality (polarization index) of the
434 cells, were normalized to suppress any dimension in order to be exempted from any scale effect. The
435 first step of our method involves PCA, which helps us determine the main parameters responsible for
436 the data dispersion. The first principal component (PC1) captures the direction of maximum variance
437 in the data, and subsequent component (PC2) captures the direction of the next highest variance
438 (Fig. 2B). Typically, the first two principal components account for a significant proportion (often over
439 70%) of the data's total variance, allowing us to reduce the dataset's complexity to a two-
440 dimensional space, such as a two-dimensional plane defined by PC1 and PC2 (Fig. 2C).

441 Next, each parameter was projected onto these principal components, which helps us rank
442 parameters based on their influence on the overall data structure (Fig. 2D). To determine the number
443 of parameters used to elaborate the ranking, we selected the median number of the normalized
444 cumulative projection (threshold = 0.5). We assign weights to the selected parameters based on their
445 projections onto PC1, which allows us to emphasize the most influential parameters. This weighted
446 projection, along with phase factors calculated for each parameter (referred as ϕ_n in the Methods
447 section), forms the basis of an Andrews Plot — a graphical representation that simplifies high-
448 dimensional data into a two-dimensional signal using trigonometric functions.

449 The Andrews Plot represents each individual microglia, as a unique curve, allowing for visual
450 comparison based on their trajectories within this synthesized signal (Fig. 2E). This method enables
451 efficient visual comparisons and insights into complex datasets with potentially significant

452 implications for data analysis and interpretation. We took advantage of this representation to rank
453 the cells based on their morphology; the ranking is established at the time point displaying the
454 highest variance, i.e. the time point where the curves are the most dispersed, also named ⍰ (Fig. 2E).

455 The obtained ranking is displayed on Fig. 3A. To evaluate the quality of the ranking method, we
456 compared the automated ranking to a subjective manual ranking by experts based on visual
457 morphological criteria (cell size; number, length and branching of the processes). To assess the
458 similarity degree between the rankings, we calculated Spearman's rank correlation coefficient
459 (r_S=0.96; Fig. 3B,E). This test revealed that the automated ranking is close to the manual ranking. To
460 ensure the reliability of the manual ranking, we compared the automated ranking with another
461 expert and obtained the same results (r_S=0.97; Fig. 3C,F). Interestingly, the comparison between the
462 two manual rankings shows similar results to those obtained when compared to the automated
463 ranking (r_S=0.93; Fig. 3D,G), indicating that variability is the same between automated or manual
464 rankings. However, automated ranking provided an objective and repeatable result, validating our
465 method. Thus, we are able to generate an accurate ranking of the cells based on morphological
466 criteria.

467 **Evaluation of MorphoCellSorter on other datasets of microglia from different animals, age, models**
468 **and imaging techniques**

469 One limitation to the use of a general and common method to characterize microglial morphology is
470 the high diversity of study material: the models (*in vivo*, *ex vivo, in vitro*, fixed or live tissue), the type
471 of collected signal (DAB or fluorescent staining, endogenous fluorescence…), the imaging technique
472 (influencing the resolution and the background noise). We thus wanted to evaluate the capacity of
473 MorphoCellSorter to accurately rank microglia from various datasets having different morphological
474 characteristics (Table 1). As previously, we compared the results to manual rankings performed by
475 two independent experts to evaluate the quality of the automated rankings (Table 1). We tested the
476 accuracy of the rankings using several thresholds impacting the number of parameters selected as

477 entries for the Andrews plots (Table 1). To maximize the accuracy of the automated ranking for all
478 datasets, we determined which threshold provided the best rankings overall (Supp. Table 1). We
479 observed that a threshold of 0.8 (Supp. Table 1), leading to 11 to 12 selected parameters (Supp. Fig.
480 1A-E), constituted a good compromise to obtain good rankings for all datasets. Thus, we chose to fix
481 this threshold for the following analyses. The Andrews plots and rankings obtained at the 0.8
482 threshold are respectively displayed in Supplemental Fig. 2 and 3.

483 Thus, our Andrews plot-based ranking method, relying on an automatic selection of relevant
484 parameters thanks to the PCA, allows a reliable automated ranking of the cells based on their
485 morphologies. The diversity of the tested datasets, with different models, types of signal and imaging
486 techniques shows that our approach offers a good sorting of the cells independently of their shape
487 and context.

488 **APPxPS1-KI microglia in the visual cortex have significant morphological alterations compared to**
489 **control cells.**

490 To determine the usability of our approach to compare microglial morphology in different conditions,
491 we used MorphoCellSorter to assess the presence of morphological alteration in the context of an
492 adult pathological murine model of Alzheimer's disease. This model is known to induce amyloid
493 plaques with dystrophic neurites, synaptic dysfunction and behavioral deficits (Casas et al., 2004).
494 We compared the morphology of PS1-KI (control) and APPxPS1-KI microglia in the visual cortex (Fig.
495 4A). Eleven parameters were automatically selected by the PCA: circularity, ramification index,
496 perimeter area ratio, fractal dimension, skeleton processes ratio, density, convexity, processes cell
497 areas ratio, lacunarity, branching index and processes soma areas ratio (Supp. Fig. 4A-C) and used to
498 generate the Andrews plots (Supp. Fig. 4D). The automated ranking obtained revealed that control
499 and APPxPS1-KI microglia were well segregated with APPxPS1-KI microglia at the beginning of the
500 ranking and control mice at the end (Fig. 4B). The distributions showed a 16.4% overlap between the

501 populations, meaning that a large number of APPxPS1-KI cells have a morphology that differs from
502 that of controls (Fig. 4C).

503 The morphological indices showed significant differences between APPxPS1-KI and control microglia.
504 The parameters measuring the morphological complexity of the cells highlighted a clear decrease in
505 the ramification level of APPxPS1-KI microglia, with for example a fractal dimension and convexity
506 decrease and a circularity increase. However, there were no significant differences in the cells'
507 linearity and polarity between groups (Fig. 4D-W).

508 Thus, this approach allowed the detection of morphological changes of microglia in the visual cortex
509 of APPxPS1-KI mice.

510 **MorphoCellSorter pinpoints no morphological alterations in a model of congenital central**
511 **hypoventilation syndrome.**

512 Congenital central congenital hypoventilation syndrome (CCHS) is a rare genetic disease is associated
513 with mutations of the PHOX2B gene and characterized by life-threatening breathing deficiencies
514 (Ceccherini, Kurek, & Weese-Mayer, 2022; Dubreuil et al., 2008). Phox2b is a transcription factor
515 required for the specification of the autonomous nervous system that contains respiratory control
516 centers. Because some of our preliminary observations strongly suggest a possible involvement of
517 microglia in the disease (unpublished data), we tested whether MorphoCellSorter highlighted
518 eventual morphological alterations of microglia in Phox2b mutants (CCHS embryos) compared to
519 wildtype embryos (WT), focusing on brainstem tissue that hosts respiratory networks involved in
520 breathing rhythmogenesis.

521 In this case using a threshold of 0.8, the PCA highlighted 12 parameters that were used to rank
522 microglia with Andrews plots: circularity, ramification index, perimeter area ratio, skeleton
523 processes ratio, fractal dimension, processes cell areas ratio, density, branching index, processes cell
524 areas ratio, convexity, lacunarity and solidity (Supp. Fig. 5A-C). These parameters were weighted to

525 generate the Andrews plots (Supp. Fig. 5D) used to rank the cells according to their morphology (Fig.
526 5B; complete ranking in Supp. Fig. 6).

527 Both populations displayed a large variability of morphologies from amoeboid to few ramified
528 processes and were well represented throughout the ranking (Fig. 5B). This is concordant with
529 previous studies on developing microglia: they can concomitantly be found in a large variety of
530 shapes and morphologies (Orłowski, Sołtys, & Janeczko, 2003). Indeed, the distributions of Andrews
531 scores showed no difference between WT and mutant mice. The overlap of distributions between
532 the populations found was 78.9% (Fig. 5C). Accordingly, when taking into consideration the various
533 morphological indices, there was no significant difference between WT and Phox2b mutant
534 microglial morphologies (Fig. 5D-W). Additional experiments are required to test whether this is
535 specific for embryonic stages and whether this is associated or not to different microglial functional
536 states.

537 **Discussion**

538 MorphoCellSorter enables the automated measurement of morphological descriptors, the
539 calculation of several non-dimensional indices, and a meaningful comparison of cell populations
540 based on their morphological characteristics. The method was initially applied to an ischemic stroke
541 model on confocal images with significant morphological changes. MorphoCellSorter was
542 subsequently tested on five different datasets with heterogeneous characteristics (various models,
543 age, imaging technique and type of collected signal), showcasing its adaptability. We then
544 successfully used our approach to compare the cells' morphology in an Alzheimer's disease context,
545 and in embryonic microglia using a CCHS model. Our method can autonomously identify the most
546 effective parameters for discriminating the studied cell set, thereby providing valuable insights into
547 microglial morphology. Additionally, it offers a useful automated ordering of cells based on a
548 combination of selected parameters using Andrews plots. This feature allows for precise positioning

549 of cells along an axis, ranging from round cells to highly branched cells, facilitating the discrimination
550 of various cell populations based on their morphologies.

551 The use of the Andrews plots offers the possibility to combine all automatically selected most
552 discriminant parameters and to weight them according to their relevance, making the rankings more
553 accurate and less subjective than only sorting the cells based on one parameter. Even if we
554 recommend a threshold at 0.8 for the number of parameters selected, as it gave good rankings for all
555 datasets we tested, we included the possibility to change this threshold if the generated ranking is
556 not satisfying, knowing that all thresholds give accurate rankings when compared to expert rankings.

557 The automated parameter selection relies on principal component analysis, which is used to
558 determine the parameters that best disperse the data. In contrast, other approaches use PCA for
559 dimensionality reduction to create new morphological parameters that are difficult to apprehend as
560 they do not refer to any physical measureclarke (Clarke et al., 2021; Heindl et al., 2018). The strength
561 of MorphoCellSorter lies in its personalized approach, with automated parameter selection adapted
562 to the dataset, making it easily applicable to segmented microglia in diverse contexts, including those
563 with distinct morphologies, such as microglia in culture or *in vivo* acquisitions. It does not require
564 program adaptation or the need to train a neural network for deep/machine learning approaches.
565 We observed that some selected parameters were consistent between all the tested datasets
566 (ramification index and perimeter area ratio for example), showing their robustness to differentiate
567 microglial cells with various morphologies. On the contrary, some parameters were never selected
568 (inertia and linearity for example). The information contained in these parameters were not
569 discriminant enough in the datasets we used in this present work, but we can imagine that they
570 would have been selected if we would have chosen a model in which microglial growth towards a
571 specific site is observed, such as focal laser injury(Davalos et al., 2005; Haynes et al., 2006).

572 We also introduce a ranking tool to further enhance morphological analysis. In contrast to recent
573 studies, we opt for ordering cells rather than classifying them. Microglial morphologies can span a

574 continuum with no clear boundaries between morphotypes. Automated clustering methods such as
575 k-means (Young & Morrison, 2018) may be more suggestive, as they require an *a priori*
576 determination of the number of clusters. Hierarchical clustering (Clarke et al., 2021) can avoid this
577 requirement but may result in non-reproducible clusters, or clusters without biological meaning.
578 Attempts to identify distinct morphotypes, as previously done with artificial intelligence (Leyh et al.,
579 2021), are also questionable due to varying definitions of morphotypes between laboratories and a
580 lack of consideration for subtle morphological differences and intermediate forms. This problem is
581 overcome by the ranking approach, as it does not lock the cells in defined categories but rather
582 position the cells in relation to one another. However, the ability to compare the evolution of
583 clusters of microglial morphologies in different conditions remains valuable, especially when
584 morphologies are heterogeneous in the same population, such as in developmental microglia or
585 pathological contexts. Comparing medians or means of certain parameters may not reveal
586 differences due to high variability, whereas comparing the evolution of the proportions of specific
587 morphotypes may provide more informative insights. The Andrews plots used to generate a ranking
588 of the cells could also be used to generate clusters of the cells presenting morphological
589 resemblances, as similar cells display similar Andrews curves' trajectories.

590 We chose not to integrate a segmentation tool into our program, as the segmentation method
591 should be tailored to the specific imaging conditions, materials, and microscopes used. Diverse
592 segmentation methods are available in different software, with varying levels of automation and
593 manual input requirements. In this work, we present methods using FIJI. It is important to note that
594 achieving perfect cell segmentation is not a prerequisite for using MorphoCellSorter since the tool
595 does not aim to provide highly precise measurements of microglial morphology. For instance,
596 discontinuous processes are not problematic. Consequently, it is possible to work with lower-
597 resolution microscopes, such as epifluorescence wide-field microscopes, although the segmentation
598 process may be more labor-intensive if the source images are of lower quality. Obviously, the results
599 of the ranking will be highly affected by the quality and the homogeneity of segmentation in a given

600 data set. However, we did not assess how much the resolution of the microscope used affects the
601 quality of the ranking as low resolution and poor signal to noise ratio would mainly affect the
602 segmentation step which is not discussed in this paper.

603 One potential limitation is that we decided to work with 2D Z-stack projections, as accurate 3D
604 reconstructions are time-consuming and require high-resolution acquisitions. Our goal was to
605 develop a fast and robust method that could be broadly applicable to most microscopes and imaging
606 scenarios. Therefore, our approach may not yield precise measurements of parameters such as the
607 exact number and length of processes or their hierarchy. However, other research groups have
608 successfully developed tools capable of providing these types of measurements, such as 3DMorph
609 (York, LeDue, Bernier, & MacVicar, 2018) and MorphOMICS via Imaris (Colombo et al., 2022). Instead,
610 MorphoCellsorter is a rapid way to determine if a treatment, genotype or location of cells affects
611 morphology without going through the laborious work of 3D reconstruction. Our tool can thus be
612 complementary to methods that provide those precise metrics.

613 In summary, MorphoCellSorter is an efficient and user-friendly tool for morphological analysis that
614 operates with minimal computation time. The code is open-source on GitHub, accessible by the
615 community (https://github.com/Pascuallab/MorphCellSorter) and improved according to the needs.
616 It can be complemented with additional measures, such as the expression of specific markers, to
617 investigate the relationship between morphology and gene expression. The emergence of spatial
618 transcriptomics is a promising avenue for furthering our understanding of the link between
619 morphology and phenotype in the microglia field in which MorphoCellSorter will be of great interest.

620 **Figure legends**

621 **Figure 1: k-means clustering identifies highly different populations contralaterally vs ipsilaterally in**
622 **an ischemic stroke model but offers a heterogeneous cluster composition.**

623 **A** T2-weighted MRI acquisition of the tMCAO rat brain 24 hours after reperfusion (top). Z maximum
624 projections of IBA1 staining of microglia on the ipsilateral side to the lesion (bottom left) and
625 contralateral side (bottom right). Scale bar: 20 µm. **B** Scatter plot with each dot representing one
626 microglia from the complete dataset (ipsilateral and contralateral), plotted in function of their PC1
627 against PC2 values from the PCA conducted on all 20 initial morphological parameters. The colors
628 represent the clusters identified by the k-means method, and the 'x' symbols are the centers of each
629 cluster. **C** All microglia from the dataset with colors associated to their affiliated cluster: green
630 corresponds to cluster 1 (ramified microglia), blue corresponds to cluster 2 (activated microglia),
631 yellow corresponds to cluster 3 (amoeboid microglia) and pink to cluster 4 (rod-like microglia). The
632 white crosses indicate cells that exhibit morophological characteristics that should categorize them in
633 another cluster. **D** Pie chart illustrating the proportion of each cluster constituting the contralateral
634 and ipsilateral sides.

635 **Figure 2**: **MorphoCellSorter approach to generate a ranking of the cells based on their morphology**
636 **applied to the ischemic stroke model on fixed tissue.**

637 **A** Summary of the fully automated MorphoCellSorter approach: morphological indexes of the
638 individualized and binarized microglia are computed on a first script (MorphoCellMeter), and the
639 resulting data table is used as an entry for MorphoCellSorter to generate the ranking of the cells
640 based on their morphological characteristics. **B** Cascade of normalized eigenvalues. The blue bars
641 represent the eigenvalues for each principal component (PCs), and the red curve is the cumulative
642 sum of the values. The first two eigenvalues corresponding to the first two PCs that account for over
643 70% of the total sum. **C** Correlation circle in the PC1 and PC2 planes. **D** Parameters ranked according
644 to their projection on PC1. Values are normalized by the highest projection value. To determine the
645 number of morphological parameters selected, here we consider the median number of the
646 normalized cumulative projection (pink curve), leading to a threshold at 0.5 (red line), and thus 7
647 kept parameters in this case. **E** Andrews plots generated with the 7 parameters weighted according

648 to their contribution onto PC1. Each curve represents one microglia in the high-dimensional space of
649 the 7 strongest parameters' projections onto PC1. The maximum variance between curves is
650 obtained at 359°.

651 **Figure 3: MorphoCellSorter offers a reliable ranking of microglia in an ischemic stroke model based**
652 **on their morphologies.**

653 **A** Automatic ranking generated by MorphoCellSorter of the 347 microglia constituting the ischemic
654 stroke model dataset. **B** Distribution of the rank difference between expert 1 manual and
655 MorphoCellSorter rankings. **C** Distribution of the rank difference between expert 2 manual and
656 MorphoCellSorter rankings. **D** Distribution of the rank difference between expert 1 and expert 2
657 manual rankings. **E** Correlation between expert 1 and MorphoCellSorter rankings. Spearman's
658 correlation coefficient Rs = 95968, p<0.0001. **F** Correlation between expert 2 and MorphoCellSorter
659 rankings. Spearman's correlation coefficient Rs = 97188, p<0.0001. **G** Correlation between expert 1
660 and expert 2 rankings. Spearman's correlation coefficient Rs = 93498, p<0.0001.

661 **Table 1: Evaluation of MorphoCellSorter rankings on highly heterogeneous datasets of microglia.**

662 The evaluation of the rankings is conducted by comparing the Spearman's correlation coefficients. w:
663 weeks, m: months, E: embryonic day, P: postnatal day, DIV: day *in vitro*, Ex: expert.

664 **Figure 4: MorphoCellSorter identifies morphological alterations in the visual cortex of APPxPS1-KI**
665 **mice.**

666 **A** Z maximum projections of IBA1 (microglia) and 4G8 (Aβ plaques) stainings of control and APPxPS1-
667 KI mice in the visual cortex. The white arrowheads point at Aβ plaques positive for 4G8, green
668 arrowheads designate ramified microglia far from Aβ plaques and red arrowheads point to highly
669 morphologically altered microglia close to Aβ plaques. Scale bar: 20µm. **B** MorphoCellSorter
670 automated ranking. Control microglia are represented in green and APPxPS1-KI microglia in orange. **C**
671 Distribution of the Andrews values at the maximum variance (Andrews scores) for control and

672 APPxPS1-KI microglia. **D-W** Morphological indexes computed by MorphoCellSorter. The data shown
673 are the mean ± standard deviation (std). Linear mixed models were applied when the application
674 conditions were respected and Wilcoxon tests were performed otherwise (for the Span Ratio) (N=3
675 mice for each condition, $n_{APP\text{-}PS1xKI}$ and $n_{Control}$ = 180). *p<0.05; **p<0.01; ***p<0.001.

676 **Figure 5: Accurate sorting of embryonic microglia reveals no morphological difference between**
677 **CCHS and WT embryos' microglia.**

678 **A** IBA1 stainings in WT and CCHS embryos' brainstems. **B** MorphoCellSorter automated ranking. WT
679 microglia are displayed in light purple and mutated microglia are represented in pink. Only every 3
680 microglia composing the dataset are displayed for readability purposes. **C** Distribution of the
681 Andrews scores for CCHS and WT microglia. **D-W** Morphological indexes computed by
682 MorphoCellSorter. The data's distribution is represented as well as the mean ± std. Linear mixed
683 models were applied (N_{WT}=5, N_{mutant}=4; n_{WT}=498 and n_{mutant}=444).

684 **Supplementary information**

685 **Supplemental figure 1: Parameters ranked according to their normalized projection onto PC1 for**
686 **the 5 tested datasets.**

687 Parameters ranked according to their projection onto PC1 for the following datasets: temporary
688 mean cerebral artery occlusion (tMCAo) on fixed tissue (**A**), permanent mean cerebral artery
689 occlusion (pMCAo) on live tissue (**B**), Alzheimer's disease (AD) model (**C**), embryonic microglia (**D**) and
690 microglia in culture (**E**). Values are normalized by the highest projection value. The number of
691 morphological parameters selected is determined by the threshold corresponding value of the
692 normalized cumulative projection selected (pink curve).

693 **Supplemental table 1: Identification of the optimal threshold.**

694 EM: Embryonic microglia, MC: Microglia in culture.

695 **Supplemental figure 2: Andrews plots at a 0.8 threshold.**

696 Andrews plots for the following datasets: temporary mean cerebral artery occlusion (tMCAo) on fixed
697 tissue (**A**), permanent mean cerebral artery occlusion (pMCAo) on live tissue (**B**), Alzheimer's disease
698 (AD) model (**C**), embryonic microglia (**D**) and microglia in culture (**E**).

699 **Supplemental figure 3: MorphoCellSorter rankings generated for the 5 datasets at a 0.8 threshold.**

700 **A** Ranking for the tMCAo fixed tissue data set, n=347 cells**.** **B** Ranking for the pMCAo live tissue data
701 set, n= 168 cells**.** **C** Ranking for the AD model data set, n=180 cells. **D** Ranking for the embryonic data
702 set, n=407 cells. **E** Ranking for microglia in culture data set, n=96

703 **Supplemental figure 4: Elaboration of MorphoCellSorter ranking for the AD dataset.**

704 **A** Cascade of normalized eigenvalues. **B** Correlation circle in the PC1 and PC2 planes. **C** Parameters
705 ranked according to their projection on PC1. Values are normalized by the highest projection value.
706 To determine the number of morphological parameters selected, we selected a threshold of 0.8 (red
707 line), and thus 11 kept parameters. **D** Andrews plots generated with the 11 parameters weighted
708 according to their contribution onto PC1. Each curve represents one microglia in the high-
709 dimensional space of the selected parameters' projections onto PC1. The maximum variance
710 between curves is obtained at 1°.

711 **Supplemental figure 5: Elaboration of MorphoCellSorter ranking for the CCHS dataset.**

712 **A** Cascade of normalized eigenvalues. **B** Correlation circle in the PC1 and PC2 planes. **C** Parameters
713 ranked according to their projection on PC1. Values are normalized by the highest projection value.
714 To determine the number of morphological parameters selected, here we used a threshold of 0.8
715 (red line), and thus 12 kept parameters. **D** Andrews plots generated with the 12 parameters
716 weighted according to their contribution onto PC1. Each curve represents one microglia in the high-
717 dimensional space of the selected parameters. The maximum variance between curves is obtained at
718 359°.

Supplemental figure 6: MorphoCellSorter automated ranking of the CCHS dataset.

WT microglia are displayed in light purple and mutated microglia are represented in pink.

Supplemental figure 7: Pre-processing and segmentation procedure for all used datasets.

Steps in grey were performed on FIJI, blue on MATLAB, yellow on ZEISS ZEN and purple on Procreate.

Supplemental figure 8: Illustration of the 20 morphological indexes automatically computed.

Ethics approval and consent to participate

Not applicable.

Consent for publication

Not applicable.

Availability of data and materials

The original code of MorphoCellSorter is available on GitHub (https://github.com/PascualLab/MorphocellSorter).

The datasets used during the current study are available from the corresponding author on reasonable request.

Competing interests

The authors declare that they have no competing interests.

Funding

This study is supported by research grants from Fondation pour la recherche médicale (reference DQ20170336751) and has been developed within the BETPSY project, which is supported by a public

grant overseen by the French national research agency (Agence nationale de la recherche, ANR), as part of the second "Investissements d´Avenir" program (reference ANR-18-RHUS-0012). This work was also supported by the French National Research Agency within the framework of the LABEX CORTEX ANR-11-LABX-0042.

Authors' contributions

SB, SMD, PM, JC and OP conceptualized and designed the study. JC and OP were in charge of overall direction. The experiments were conducted by SB, MTB, LC, BP, GP CL, IH, VH, MW and SM. JH and OP secured the fundings. Coding was executed by SB, SMD, PM and JC. SB, PDG and KC participated in the analysis. All authors provided critical feedback and helped shape the research, analysis and manuscript. SB and OP drafted the manuscript, and all authors provided critical review, commentary or revision.

Acknowledgments

We acknowledge the contribution of SFR Santé Lyon-Est (UAR3453 CNRS, US7 Inserm, UCBL) facility: CIQLE (a LyMIC member), especially Bruno Chapuis and Denis Ressnikoff for their help.

References

A, C. (2023). Hausdorff (Box-Counting) Fractal Dimension.

Adaikkan, C., Middleton, S. J., Marco, A., Pao, P. C., Mathys, H., Kim, D. N., . . . Tsai, L. H. (2019). Gamma Entrainment Binds Higher-Order Brain Regions and Offers Neuroprotection. *Neuron, 102*(5), 929-943.e928. doi:10.1016/j.neuron.2019.04.011

Adeluyi, A., Guerin, L., Fisher, M. L., Galloway, A., Cole, R. D., Chan, S. S. L., . . . Turner, J. R. (2019). Microglia morphology and proinflammatory signaling in the nucleus accumbens during nicotine withdrawal. *Science Advances, 5*(10), eaax7031. doi:10.1126/sciadv.aax7031

768 Ali, S., Liu, X., Queen, N. J., Patel, R. S., Wilkins, R. K., Mo, X., & Cao, L. (2019). Long-term
769 environmental enrichment affects microglial morphology in middle age mice. *Aging, 11*(8),
770 2388-2402. doi:10.18632/aging.101923
771 Amiel, J., Laudier, B., Attié-Bitach, T., Trang, H., de Pontual, L., Gener, B., . . . Lyonnet, S. (2003).
772 Polyalanine expansion and frameshift mutations of the paired-like homeobox gene PHOX2B
773 in congenital central hypoventilation syndrome. *Nature Genetics, 33*(4), 459-461.
774 doi:10.1038/ng1130
775 Andrews, D. F. (1972). Plots of High-Dimensional Data. *Biometrics, 28*(1), 125-136.
776 doi:10.2307/2528964
777 Anttila, J. E., Whitaker, K. W., Wires, E. S., Harvey, B. K., & Airavaara, M. (2017). Role of microglia in
778 ischemic focal stroke and recovery: focus on Toll-like receptors. *Progress in neuro-*
779 *psychopharmacology & biological psychiatry, 79*(Pt A), 3-14.
780 doi:10.1016/j.pnpbp.2016.07.003
781 Arganda-Carreras, I., Kaynig, V., Rueden, C., Eliceiri, K. W., Schindelin, J., Cardona, A., & Sebastian
782 Seung, H. (2017). Trainable Weka Segmentation: a machine learning tool for microscopy pixel
783 classification. *Bioinformatics, 33*(15), 2424-2426. doi:10.1093/bioinformatics/btx180
784 Bohlen, C. J., Bennett, F. C., & Bennett, M. L. (2019). Isolation and culture of microglia. *Current*
785 *protocols in immunology, 125*(1), e70. doi:10.1002/cpim.70
786 Casas, C., Sergeant, N., Itier, J.-M., Blanchard, V., Wirths, O., van der Kolk, N., . . . Pradier, L. (2004).
787 Massive CA1/2 neuronal loss with intraneuronal and N-terminal truncated Abeta42
788 accumulation in a novel Alzheimer transgenic model. *The American Journal of Pathology,*
789 *165*(4), 1289-1300. doi:10.1016/s0002-9440(10)63388-3
790 Ceccherini, I., Kurek, K. C., & Weese-Mayer, D. E. (2022). Developmental disorders affecting the
791 respiratory system: CCHS and ROHHAD. *Handb Clin Neurol, 189*, 53-91. doi:10.1016/B978-0-
792 323-91532-8.00005-7

Choi, S., Hill, D., Guo, L., Nicholas, R., Papadopoulos, D., & Cordeiro, M. F. (2022). Automated characterisation of microglia in ageing mice using image processing and supervised machine learning algorithms. *Scientific Reports, 12*(1), 1806. doi:10.1038/s41598-022-05815-6

Clarke, D., Crombag, H. S., & Hall, C. N. (2021). An open-source pipeline for analysing changes in microglial morphology. *Open Biology, 11*(8), 210045. doi:10.1098/rsob.210045

Colombo, G., Cubero, R. J. A., Kanari, L., Venturino, A., Schulz, R., Scolamiero, M., . . . Siegert, S. (2022). A tool for mapping microglial morphology, morphOMICs, reveals brain-region and sex-dependent phenotypes. *Nature Neuroscience, 25*(10), 1379-1393. doi:10.1038/s41593-022-01167-6

Davalos, D., Grutzendler, J., Yang, G., Kim, J. V., Zuo, Y., Jung, S., . . . Gan, W.-B. (2005). ATP mediates rapid microglial response to local brain injury in vivo. *Nature Neuroscience, 8*(6), 752-758. doi:10.1038/nn1472

Dubreuil, V., Ramanantsoa, N., Trochet, D., Vaubourg, V., Amiel, J., Gallego, J., . . . Goridis, C. (2008). A human mutation in Phox2b causes lack of CO2 chemosensitivity, fatal central apnea, and specific loss of parafacial neurons. *Proc Natl Acad Sci U S A, 105*(3), 1067-1072. doi:10.1073/pnas.0709115105

Fernández-Arjona, M. d. M., Grondona, J. M., Granados-Durán, P., Fernández-Llebrez, P., & López-Ávalos, M. D. (2017). Microglia Morphological Categorization in a Rat Model of Neuroinflammation by Hierarchical Cluster and Principal Components Analysis. *Front Cell Neurosci, 11*, 235. doi:10.3389/fncel.2017.00235

Fumagalli, S., Perego, C., Ortolano, F., & De Simoni, M.-G. (2013). CX3CR1 deficiency induces an early protective inflammatory environment in ischemic mice. *Glia, 61*(6), 827-842. doi:10.1002/glia.22474

García-Osorio, C., & Fyfe, C. (2005). Visualization of High-dimensional Data via Orthogonal Curves. *JUCS - Journal of Universal Computer Science, 11*((11)), 1806-1819. doi:10.3217/jucs-011-11-1806

Hanisch, U.-K., & Kettenmann, H. (2007). Microglia: active sensor and versatile effector cells in the normal and pathologic brain. *Nat Neurosci, 10*(11), 1387-1394.

Haynes, S. E., Hollopeter, G., Yang, G., Kurpius, D., Dailey, M. E., Gan, W. B., & Julius, D. (2006). The P2Y12 receptor regulates microglial activation by extracellular nucleotides. *Nat Neurosci, 9*(12), 1512-1519.

Heindl, S., Gesierich, B., Benakis, C., Llovera, G., Duering, M., & Liesz, A. (2018). Automated Morphological Analysis of Microglia After Stroke. *Front Cell Neurosci, 12*. doi:10.3389/fncel.2018.00106

Hubert, V., Hristovska, I., Karpati, S., Benkeder, S., Dey, A., Dumot, C., . . . Wiart, M. (2021). Multimodal Imaging with NanoGd Reveals Spatiotemporal Features of Neuroinflammation after Experimental Stroke. *Adv Sci (Weinh), 8*(17), e2101433. doi:10.1002/advs.202101433

Hubert, V., Hristovska, I., Karpati, S., Benkeder, S., Dey, A., Dumot, C., . . . Wiart, M. (2021). Multimodal Imaging with NanoGd Reveals Spatiotemporal Features of Neuroinflammation after Experimental Stroke. *Adv Sci (Weinh), 8*(17), e2101433. doi:10.1002/advs.202101433

Jolliffe, I. T., & Cadima, J. (2016). Principal component analysis: a review and recent developments. *Philosophical Transactions. Series A, Mathematical, Physical, and Engineering Sciences, 374*(2065), 20150202. doi:10.1098/rsta.2015.0202

Kettenmann, H., Hanisch, U.-K., Noda, M., & Verkhratsky, A. (2011). *Physiology of Microglia* (Vol. 91).

Kongsui, R., Beynon, S. B., Johnson, S. J., & Walker, F. R. (2014). Quantitative assessment of microglial morphology and density reveals remarkable consistency in the distribution and morphology of cells within the healthy prefrontal cortex of the rat. *J Neuroinflammation, 11*, 182. doi:10.1186/s12974-014-0182-7

Leyh, J., Paeschke, S., Mages, B., Michalski, D., Nowicki, M., Bechmann, I., & Winter, K. (2021). Classification of Microglial Morphological Phenotypes Using Machine Learning. *Front Cell Neurosci, 15*, 701673. doi:10.3389/fncel.2021.701673

Madry, C., Kyrargyri, V., Arancibia-Cárcamo, I. L., Jolivet, R., Kohsaka, S., Bryan, R. M., & Attwell, D. (2018). Microglial Ramification, Surveillance, and Interleukin-1β Release Are Regulated by the Two-Pore Domain K+ Channel THIK-1. *Neuron, 97*(2), 299-312.e296. doi:10.1016/j.neuron.2017.12.002

Morrison, H., Young, K., Qureshi, M., Rowe, R. K., & Lifshitz, J. (2017). Quantitative microglia analyses reveal diverse morphologic responses in the rat cortex after diffuse brain injury. *Scientific Reports, 7*(1), 13211. doi:10.1038/s41598-017-13581-z

Nimmerjahn, A., Kirchhoff, F., & Helmchen, F. (2005). Resting microglial cells are highly dynamic surveillants of brain parenchyma in vivo. *Science, 308*(5726), 1314-1318.

Orłowski, D., Sołtys, Z., & Janeczko, K. (2003). Morphological development of microglia in the postnatal rat brain. A quantitative study. *International Journal of Developmental Neuroscience: The Official Journal of the International Society for Developmental Neuroscience, 21*(8), 445-450. doi:10.1016/j.ijdevneu.2003.09.001

Paolicelli, R. C., Sierra, A., Stevens, B., Tremblay, M.-E., Aguzzi, A., Ajami, B., . . . Wyss-Coray, T. (2022). Microglia states and nomenclature: A field at its crossroads. *Neuron, 110*(21), 3458-3483. doi:10.1016/j.neuron.2022.10.020

Plescher, M., Seifert, G., Hansen, J. N., Bedner, P., Steinhäuser, C., & Halle, A. (2018). Plaque-dependent morphological and electrophysiological heterogeneity of microglia in an Alzheimer's disease mouse model. *Glia, 66*(7), 1464-1480. doi:10.1002/glia.23318

R, B. (2023). Thresholding Tool.

Sierra, A., Abiega, O., Shahraz, A., & Neumann, H. (2013). Janus-faced microglia: beneficial and detrimental consequences of microglial phagocytosis. *Front Cell Neurosci, 7*, 6. doi:10.3389/fncel.2013.00006

T, V. (2023). Lacunarity of a binary image.

Tolle, C. R., McJunkin, T. R., & Gorsich, D. J. (2008). An efficient implementation of the gliding box lacunarity algorithm. *Physica D: Nonlinear Phenomena, 237*(3), 306-315. doi:10.1016/j.physd.2007.09.017

Verdonk, F., Roux, P., Flamant, P., Fiette, L., Bozza, F. A., Simard, S., . . . Danckaert, A. (2016). Phenotypic clustering: a novel method for microglial morphology analysis. *J Neuroinflammation, 13*, 153. doi:10.1186/s12974-016-0614-7

Vidal-Itriago, A., Radford, R. A. W., Aramideh, J. A., Maurel, C., Scherer, N. M., Don, E. K., . . . Morsch, M. (2022). Microglia morphophysiological diversity and its implications for the CNS. *Frontiers in Immunology, 13*, 997786. doi:10.3389/fimmu.2022.997786

York, E. M., LeDue, J. M., Bernier, L.-P., & MacVicar, B. A. (2018). 3DMorph Automatic Analysis of Microglial Morphology in Three Dimensions from Ex Vivo and In Vivo Imaging. *eNeuro, 5*(6), ENEURO.0266-0218.2018. doi:10.1523/ENEURO.0266-18.2018

Young, K., & Morrison, H. (2018). Quantifying Microglia Morphology from Photomicrographs of Immunohistochemistry Prepared Tissue Using ImageJ. *Journal of Visualized Experiments: JoVE*(136), 57648. doi:10.3791/57648

Zhang, S. (2019). Microglial activation after ischaemic stroke. *Stroke and Vascular Neurology, 4*(2), 71-74. doi:10.1136/svn-2018-000196

Figure 1

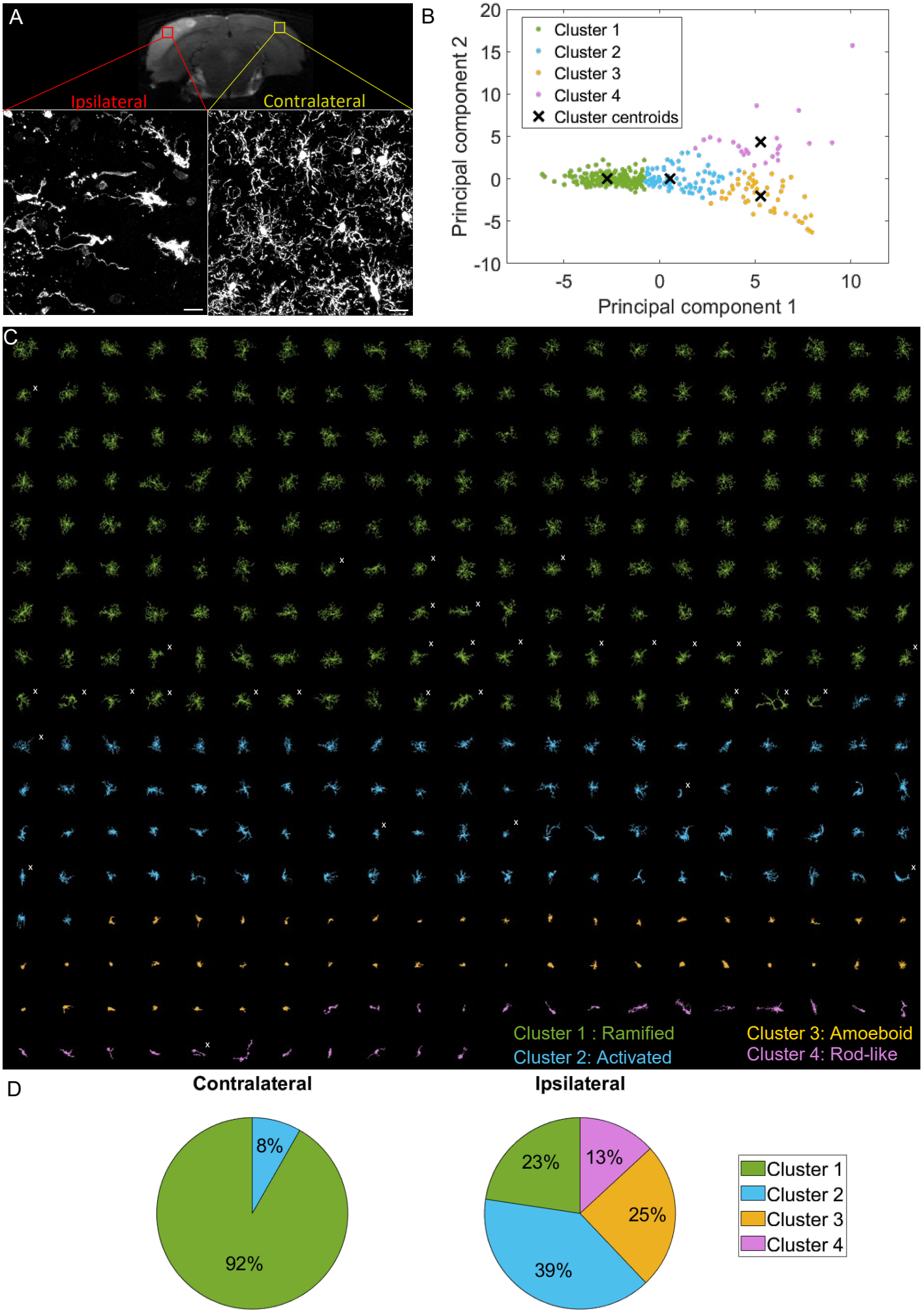
A
Ipsilateral
Contralateral
B
Cluster 1
Cluster 2
Cluster 3
Cluster 4
Cluster centroids
Principal component 2
Principal component 1
20
15
10
5
0
-5
-10
-5
0
5
10
C
Cluster 1 : Ramified
Cluster 2: Activated
Cluster 3: Amoeboid
Cluster 4: Rod-like
D
Contralateral
8%
92%
Ipsilateral
23%
13%
25%
39%
Cluster 1
Cluster 2
Cluster 3
Cluster 4

Figure 2

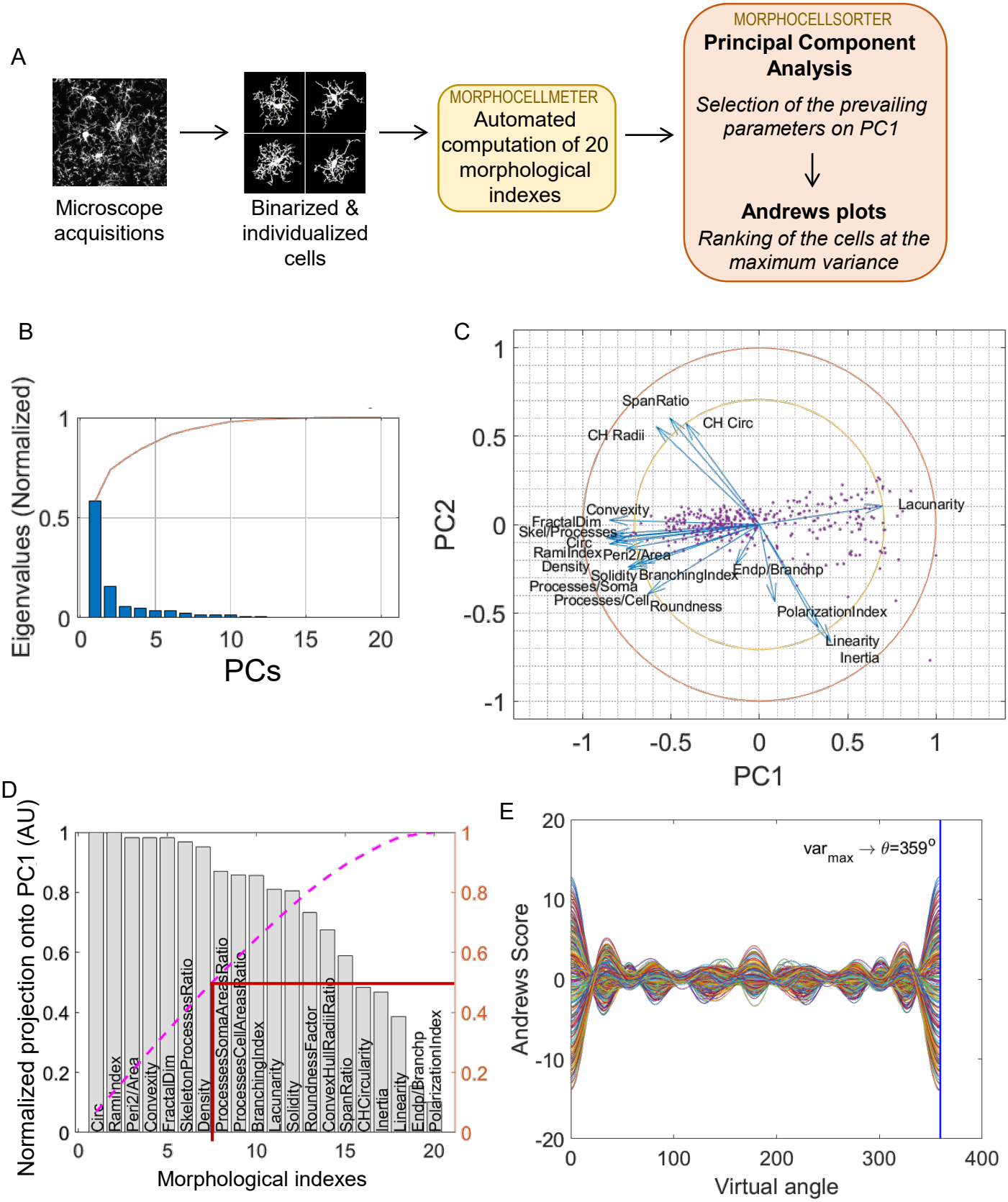
A
Microscope acquisitions
Binarized & individualized cells
MORPHOCELLMETER
Automated computation of 20 morphological indexes
MORPHOCELLSORTER
Principal Component Analysis
Selection of the prevailing parameters on PC1
Andrews plots
Ranking of the cells at the maximum variance
B
Eigenvalues (Normalized)
PCs
C
PC2
PC1
SpanRatio
CH Circ
CH Radii
Convexity
FractalDim
Skel/Processes
Circ
RamiIndex
Peri2/Area
Density
Solidity
BranchingIndex
Endp/Branchp
Processes/Soma
Processes/Cell
Roundness
PolarizationIndex
Lacunarity
Linearity
Inertia
D
Normalized projection onto PC1 (AU)
Morphological indexes
Circ
RamiIndex
Peri2/Area
Convexity
FractalDim
SkeletonProcessesRatio
Density
ProcessesSomaAreasRatio
ProcessesCellAreasRatio
BranchingIndex
Lacunarity
Solidity
RoundnessFactor
ConvexHullRadiiRatio
SpanRatio
CHCircularity
Inertia
Linearity
Endp/Branchp
PolarizationIndex
E
Andrews Score
Virtual angle
var max → θ=359°

Figure 3

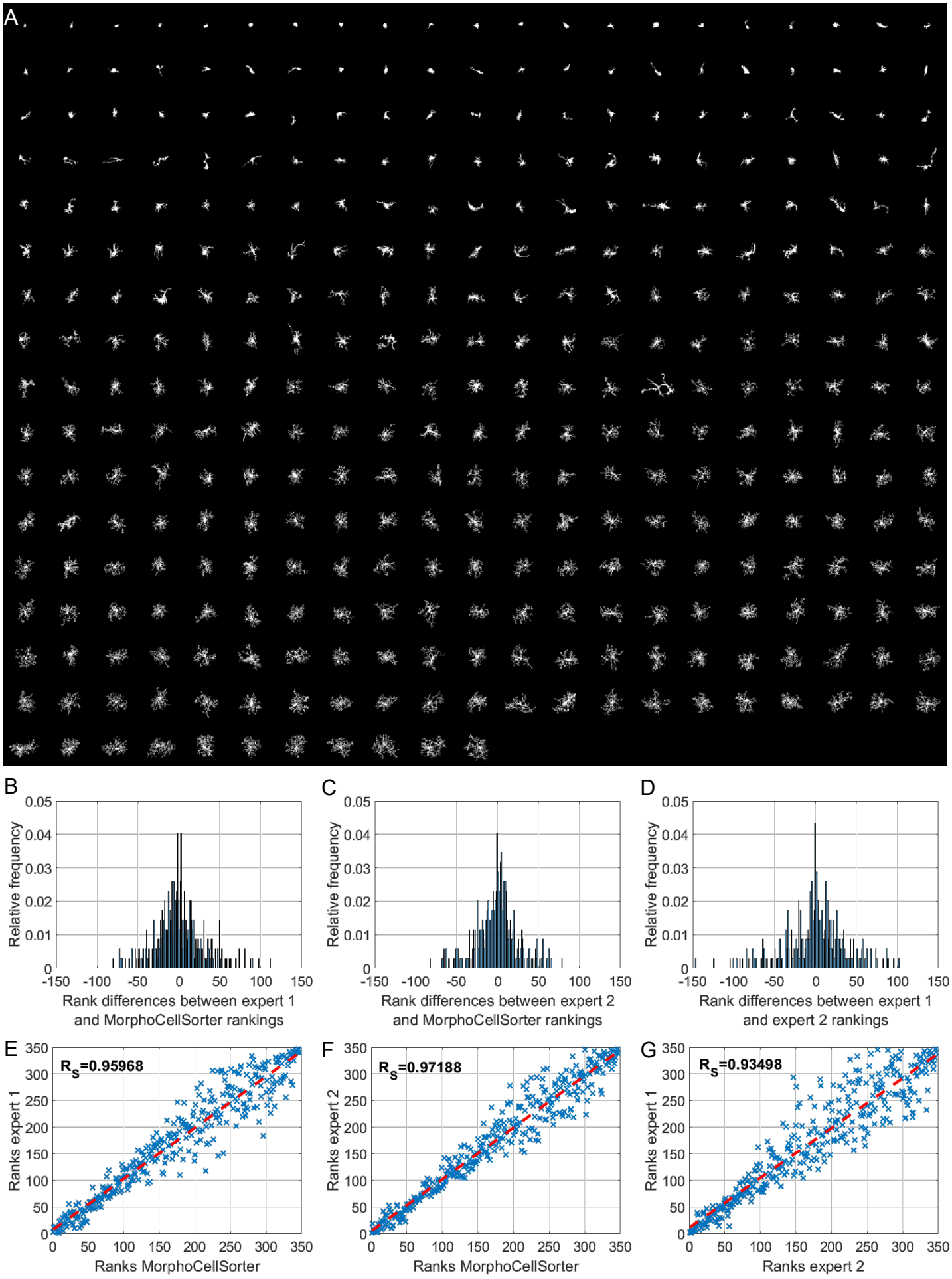
A
B
Relative frequency
Rank differences between expert 1 and MorphoCellSorter rankings
C
Relative frequency
Rank differences between expert 2 and MorphoCellSorter rankings
D
Relative frequency
Rank differences between expert 1 and expert 2 rankings
E
R_S=0.95968
Ranks expert 1
Ranks MorphoCellSorter
F
R_S=0.97188
Ranks expert 2
Ranks MorphoCellSorter
G
R_S=0.93498
Ranks expert 1
Ranks expert 2

Figure 4

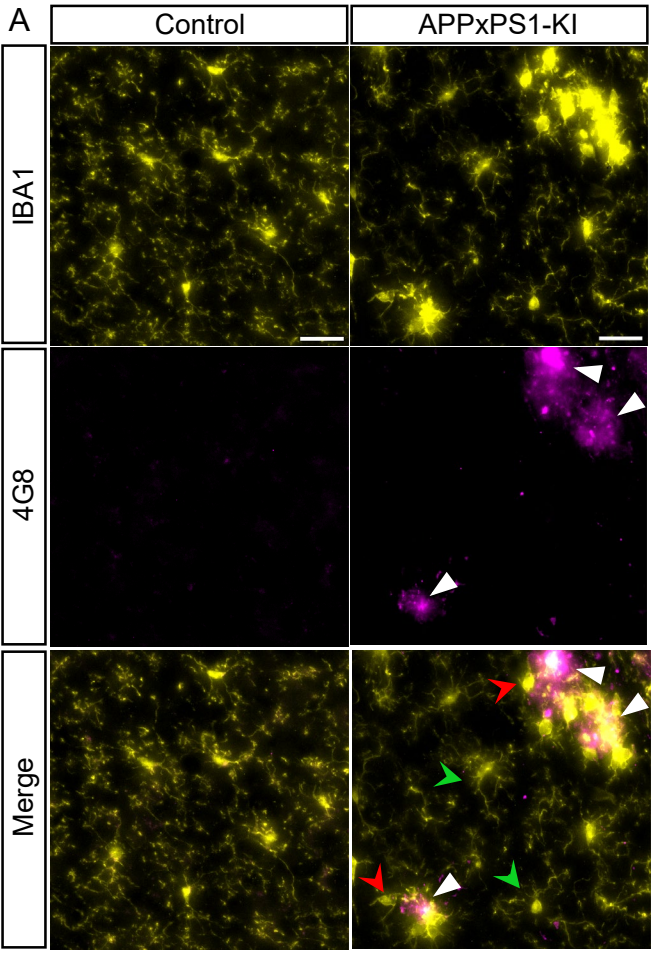
A
Control
APPxPS1-KI
IBA1
4G8
Merge

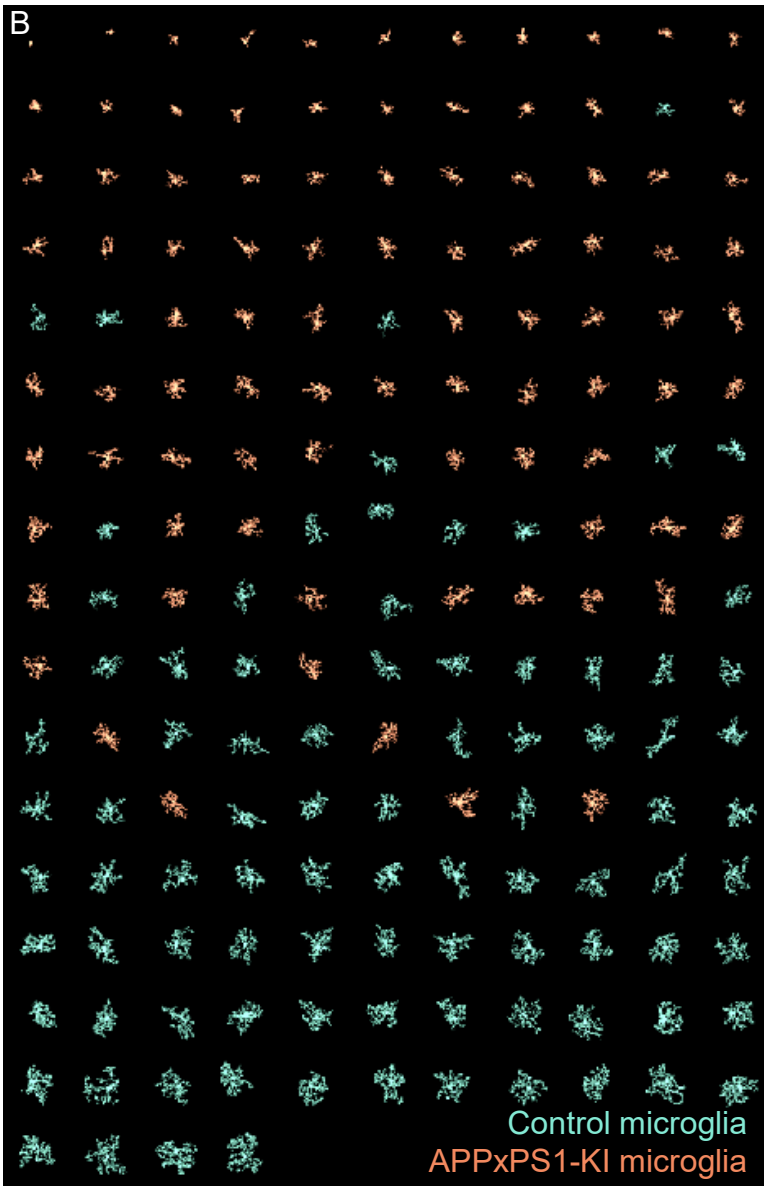
B
Control microglia
APPxPS1-KI microglia

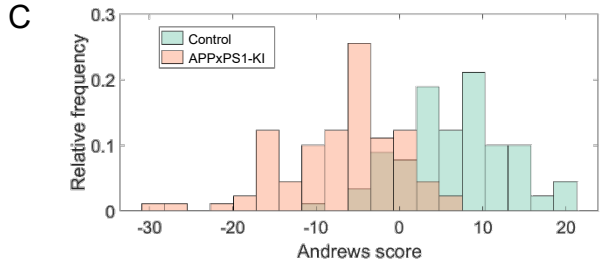
C
Control
APPxPS1-KI
Relative frequency
Andrews score

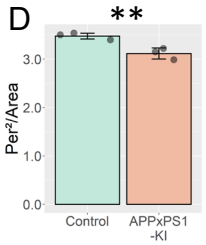
D
Per²/Area
Control
APPxPS1 -KI

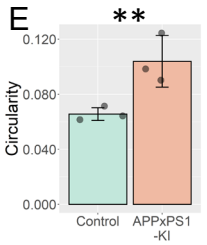
E
Circularity
Control
APPxPS1 -KI

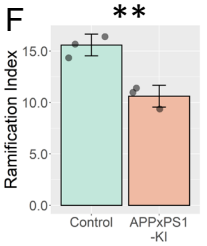
F
Ramification Index
Control
APPxPS1 -KI

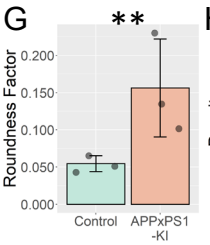
G
Roundness Factor
Control
APPxPS1 -KI

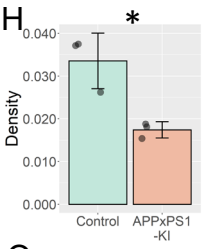
H
Density
Control
APPxPS1 -KI

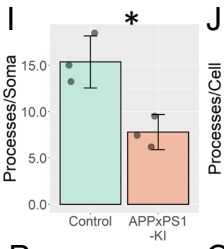
I
Processes/Soma
Control
APPxPS1 -KI

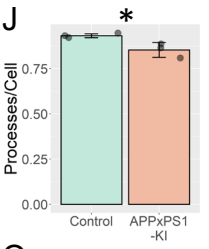
J
Processes/Cell
Control
APPxPS1 -KI

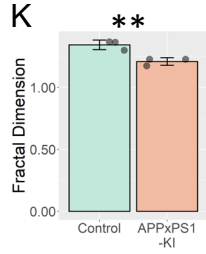
K
Fractal Dimension
Control
APPxPS1 -KI

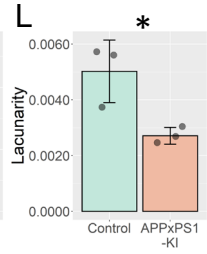
L
Lacunarity
Control
APPxPS1 -KI

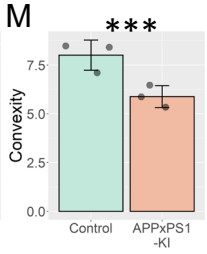
M
Convexity
Control
APPxPS1 -KI

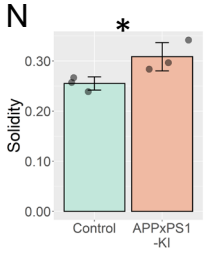
N
Solidity
Control
APPxPS1 -KI

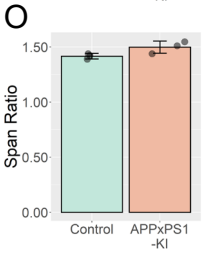
O
Span Ratio
Control
APPxPS1 -KI

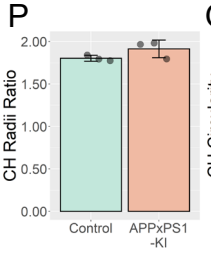
P
CH Radii Ratio
Control
APPxPS1 -KI

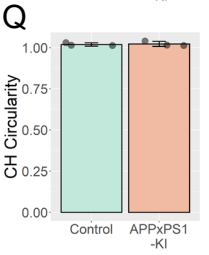
Q
CH Circularity
Control
APPxPS1 -KI

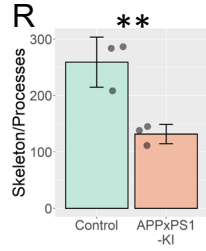
R
Skeleton/Processes
Control
APPxPS1 -KI

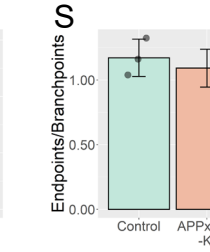
S
Endpoints/Branchpoints
Control
APPxPS1 -KI

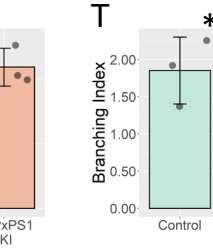
T
Branching Index
Control
APPxPS1 -KI

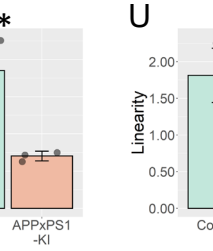
U
Linearity
Control
APPxPS1 -KI

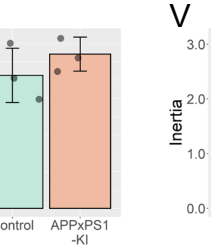
V
Inertia
Control
APPxPS1 -KI

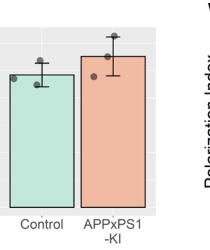
W
Polarization Index
Control
APPxPS1 -KI

Figure 5

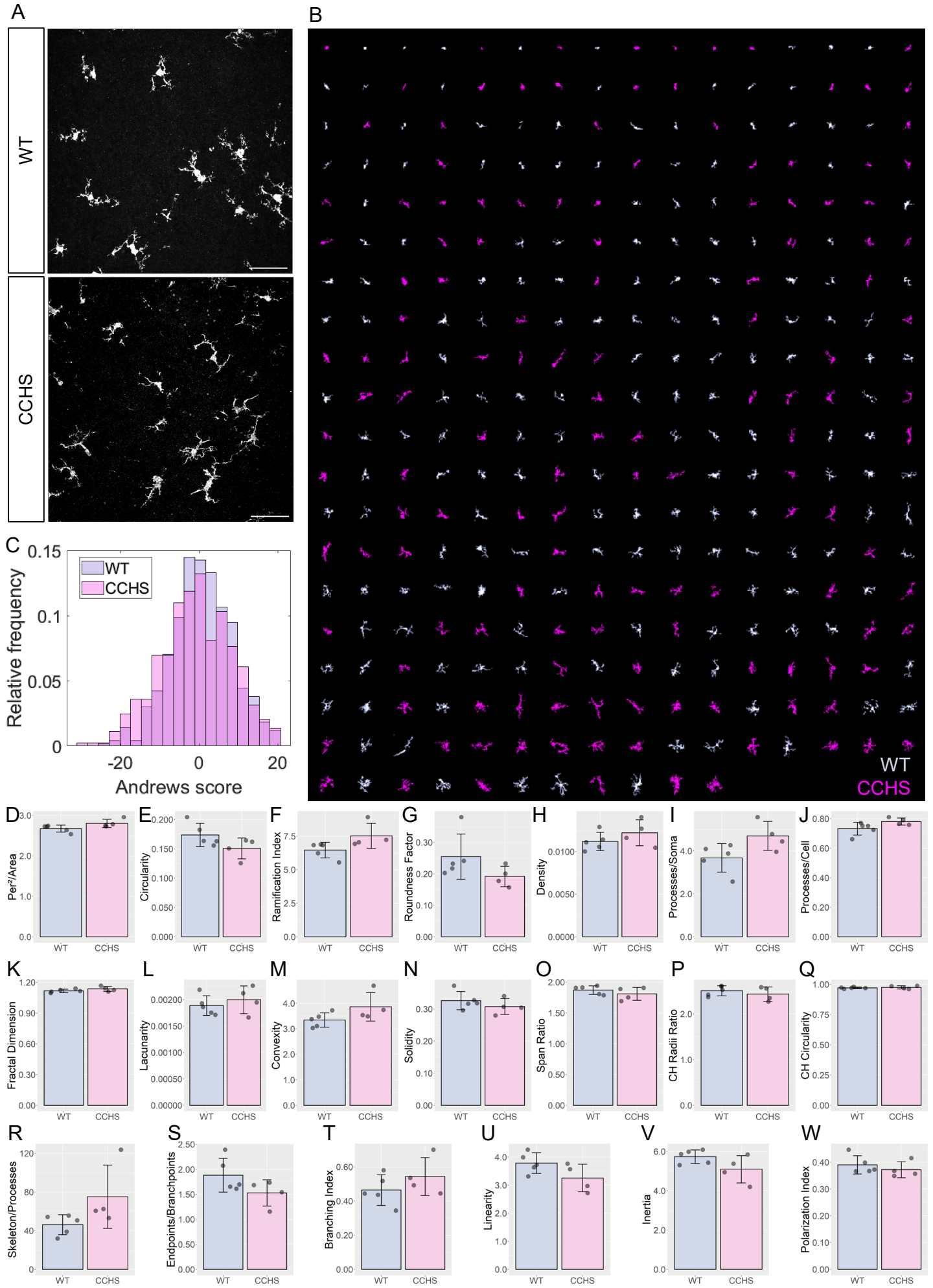
A
WT
CCHS
B
WT
CCHS
C
Relative frequency
Andrews score
WT
CCHS
D
Per²/Area
E
Circularity
F
Ramification Index
G
Roundness Factor
H
Density
I
Processes/Soma
J
Processes/Cell
K
Fractal Dimension
L
Lacunarity
M
Convexity
N
Solidity
O
Span Ratio
P
CH Radii Ratio
Q
CH Circularity
R
Skeleton/Processes
S
Endpoints/Branchpoints
T
Branching Index
U
Linearity
V
Inertia
W
Polarization Index

Table 1

Model	tMCAo fixed tissue	pMCAo live tissue	AD model	Embryonic microglia	Microglia in culture
	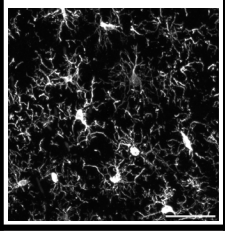	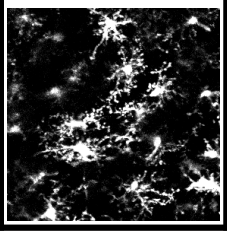	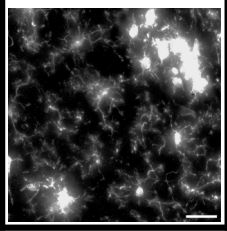	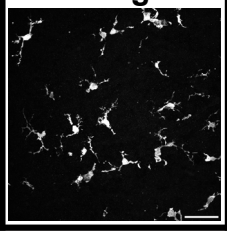	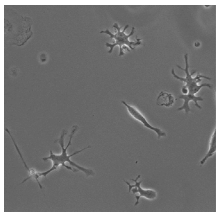
DATASETS' CHARACTERISTICS					
Animals	Male rat 7w.	Male mice 8-12 w.	Female mice 5 m.	Mice embryos E18.5	Mice pups P10 (DIV4-10)
Collected signal	IBA1 immuno-fluorescent staining	Endogenous fluorescence CX3CR1$^{GFP/+}$	IBA1 immuno-fluorescent staining	IBA1 immuno-fluorescent staining	Brightfield
Imaging technique	Confocal (40X)	Two-photon (20X)	Widefield (20X)	Confocal (40X)	BioStation (40X)
Fixed/live tissue	Fixed tissue	Live tissue	Fixed tissue	Fixed tissue	Live tissue
Number of cells	n=347	n=168	n=180	n=407	n=96

EVALUATION OF MORPHOCELLSORTER RANKINGS CORRELATION WITH MANUAL RANKINGS

	Expert	Ex 1	Ex 2	Ex 1	Ex 2	Ex 1	Ex 2	Ex 1	Ex 2	Ex 1	Ex 2
Thresholds	0.2	0.965	0.958	0.945	0.945	0.952	0.934	0.914	0.885	0.854	0.749
	0.3	0.964	0.954	0.944	9.946	0.953	0.942	0.914	0.885	0.854	0.749
	0.4	0.964	0.964	0.935	0.938	0.949	0.947	0.929	0.909	0.845	0.744
	0.5	0.96	0.972	0.938	0.939	0.943	0.945	0.927	0.907	0.877	0.837
	0.6	0.959	0.968	0.944	0.941	0.95	0.944	0.918	0.889	0.869	0.869
	0.7	0.954	0.969	0.943	0.938	0.947	0.947	0.926	0.914	0.865	0.859
	0.8	0.954	0.967	0.94	0.937	0.952	0.943	0.926	0.917	0.848	0.91
	0.9	0.95	0.959	0.929	0.929	0.95	0.944	0.922	0.92	0.851	0.91
	1	0.95	0.959	0.922	0.923	0.954	0.946	0.913	0.923	0.846	0.906
Ex 1 vs Ex 2		0.935		0.946		0.892		0.912		0.76	